Journal of
Materials Chemistry A

ROYAL SOCIETY
OF CHEMISTRY

PAPER

View Article Online
View Journal

Check for updates

Cite this: DOI: 10.1039/d5ta03712c

High-performance hydrophobic MOFs for selective acetone capture under humid conditions†

Sabrina Grigoletto,[ab] Kavosh Karami,[c] Iago Maye,[d] Ajay Padunnappattu,[e] Siddharth Ravichandran,[b] Mohammad Wahiduzzaman,[a] Louis Vanduyfhuys,[b] Veronique Van Speybroeck,[b] Matthias Thommes,[d] Joeri F. M. Denayer,[c] Norbert Stock*[e] and Guillaume Maurin*[af]

Received 9th May 2025
Accepted 10th July 2025

DOI: 10.1039/d5ta03712c

rsc.li/materials-a

Capturing acetone, a major indoor air pollutant, under humid conditions is a longstanding challenge in materials science. The key obstacle lies in finding porous adsorbents that simultaneously exhibit strong affinity for acetone and intrinsic hydrophobicity, a rare and elusive pairing. Leveraging the structural and chemical versatility of metal–organic frameworks (MOFs), we first explored a diverse set of MOFs using force field Monte Carlo and density-functional theory calculations. This computational strategy identified CAU-11(Al) as a top performer: a hydrophobic, small pore MOF that enables both high acetone affinity and uptake at trace concentrations with excellent selectivity over water. Experimental validation through gas-phase pulse chromatography, adsorption measurements, and breakthrough studies confirmed the outstanding performance of this sorbent under competitive acetone/water conditions. These results position CAU-11(Al) as a promising material for real-world acetone capture in humid indoor environments.

1 Introduction

Air pollution is not an isolated issue; it is a key disruptor of the ecological balance vital to all life on Earth. The rapid expansion of industrialization and urbanization, along with the widespread and unregulated use of chemical products has intensified this crisis. While significant efforts have been directed towards understanding and mitigating outdoor air pollution, the indoor air quality (IAQ) remains an often-overlooked concern.[1] For instance, common sources such as household appliances, building materials, paints, and cleaning agents emit volatile organic compounds (VOCs), which represent a major class of indoor air pollutants and significantly degrade IAQ.[2,3] These VOCs, characterized by their high volatility and toxicity, pose significant health risks and require the development of effective capture strategies.[4,5]

Among VOCs, acetone is a commonly used compound that functions as an essential precursor in chemical synthesis and is widely employed as a solvent across a broad range of commercial products.[6,7] Reports indicate a minimal risk level (MRL) of 8 ppm for acute exposure to acetone.

The primary health effects of acetone inhalation include respiratory tract damage and neurological symptoms. Exposure to concentrations as low as 100 ppm can cause irritation of the nose, throat, and trachea, while levels around 237 ppm may result in neurobehavioral effects such as delayed visual reaction time, weakness, and even severe narcosis.[8] Extensively used in paints, coatings, cleaning agents, and personal care products, this solvent can accumulate in enclosed environments during indoor activities such as home renovations or cleaning.

Like other VOCs, physisorption-based processes using porous adsorbents are particularly compelling for acetone capture which offer operational simplicity.[9] Microporous materials such as zeolites, and metal–organic frameworks (MOFs) have been explored as sorbents for different VOCs capture,[10–16] including acetone.[17–21] Among the zeolites, the small pore CHA, MFI, and STT in their pure silica forms show rather low acetone uptake while NaY is too hydrophilic for a selective acetone capture.[20,22] In particular, MOFs, a class of crystalline hybrid porous materials, have garnered significant attention for a wide range of adsorption/separation processes in liquid, vapor and gas phases owing to their unique richness in terms of chemical and topological diversity.[23–27] The so-called reticular concept allows for the engineering of suitable porous frameworks with desirable surface functionalities and pore size/

---

[a] ICGM, University of Montpellier, CNRS, ENSCM, Montpellier, 34293, France. E-mail: guillaume.maurin1@umontpellier

[b] Center for Molecular Modeling, Ghent University, Technologiepark 46, 9052 Zwijnaarde, Belgium

[c] Department of Chemical Engineering, Vrije Universiteit Brussel, Pleinlaan 2, 1050 Brussels, Belgium

[d] Institution of Separation Science and Technology, Friedrich-Alexander-Universität Erlangen-Nürnberg (FAU), Egerlandstr. 3, Erlangen 91058, Germany

[e] Institut für Anorganische Chemie, Christian-Albrechts-Universität zu Kiel, 24118 Kiel, Germany. E-mail: stock@ac.uni-kiel.de

[f] Institut Universitaire de France, France

† Electronic supplementary information (ESI) available. See DOI: https://doi.org/10.1039/d5ta03712c

shape to maximize host–guest interactions. Typically, the pore surface functionality can be tuned *via* the consideration of open metal sites (OMS), or through the functionalization of either the inorganic nodes or the organic linkers.[28–31] This engineering strategy has proven highly effective in enhancing adsorption and separation processes at low pressures, even at trace concentrations, for a wide range of VOCs of interest.[14,32,33] Fine-tuning the pore chemistry of MOFs can be further complemented by tailoring the pore size and shape to optimize confinement effects for specific guest molecules.

In recent years, a diverse set of MOFs has been explored for acetone capture, leveraging distinct adsorption mechanisms. ZIF-90, incorporating aldehyde-functionalized imidazolate linkers, shows high acetone affinity, with an adsorption enthalpy of -57.9 kJ mol^{-1}, resulting from interactions between acetone oxygen atom and the linker's aldehyde function delimiting the pore windows.[34] Similarly, ZIF-71 can effectively capture acetone owing to specific interactions between the acetone molecules and its chloro-functionalized imidazolate linkers.[35] Moreover, the cage-like structure of ZIFs may also contribute to their high acetone affinity through additional confinement effects. MIL-125-NH_2(Ti) demonstrates one of the highest reported acetone adsorption enthalpies of -91 kJ mol^{-1} at low coverage, resulting from strong hydrogen bonding between acetone's carbonyl group and the $-NH_2$ sites.[17] UiO-66(Zr) equally shows high affinity for acetone, with DFT-derived interaction energies reaching up to -87.5 kJ mol^{-1} associated to a preferential adsorption of acetone towards the μ-OH groups.[36] The integration of UiO-66(Zr) into sensors, capable of detecting acetone concentrations above 4 ppm, further confirmed its strong interaction potential with acetone.[37] Beyond linker functionalization, MOFs incorporating OMS provide an alternative adsorption mechanism, offering strong coordination sites between OMS and acetone. For example, the mesoporous MIL-101(Cr) demonstrates high acetone sorption uptake likely associated with strong interactions between acetone and Cr^{3+} OMS.[19]

Moreover, when considering the adsorption of polar molecules such as acetone under indoor air conditions, the selected adsorbents must be highly selective to acetone in the presence of humidity, typically for a relative humidity (RH) ranging from 30 to 60%.[38] Apart from the rare example of Fe^{3+} OMS containing MOF MIL-100(Fe), which exceptionally maintains diverse VOCs capture efficiencies even in the presence of water,[14] hydrophilic MOFs generally show a drastic drop of their VOCs sorption performances due to a competitive adsorption in favor of H_2O.[39] For instance, the presence of 10% RH was shown to substantially decrease the acetone adsorption in MOF-177 while a loss of crystallinity and porosity was observed under higher humidity conditions.[18,40] Additionally, although the aforementioned MOFs, such as UiO-66(Zr), MIL-125-NH_2(Ti) and MIL-101(Cr), have demonstrated efficacy in sensing or capturing acetone, the impact of water on their adsorption performance has not been thoroughly addressed. The availability of hydrophilic –OH/–NH_2 functions or the presence of OMS within these structures may hinder acetone capture in the presence of humidity. Alternatively, hydrophobic coating of the external surface of hydrophilic MOFs can be envisaged to circumvent this drawback; however, it requires additional processing steps.[41–43] Therefore intrinsically hydrophobic MOFs should be privileged for an efficient VOC capture in presence of water. The pore hydrophobicity of this class of porous materials is generally controlled by grafting apolar functions to the organic ligands[44] such as halogenated, alkyl, or aryl groups that can effectively reduce water adsorption.[45] However, it often comes at the cost of decreased available surface area/pore volume that can limit the adsorption uptake of VOCs like acetone.[3,33]

In this study, we deployed a joint computational/experimental approach to identify a MOF that can selectively capture acetone under humidity, encountered in indoor air conditions. Initially a series of MOFs with different pore size/shape/chemistry was computationally explored using a combination of force field (FF) Monte Carlo (MC) and density-functional theory (DFT) calculations. These molecular simulations identified CAU-11(Al),[46] a sulfone-functionalized MOF with lozenge-shaped pores, as a promising adsorbent. Its predicted high acetone affinity and large sorption uptake at low concentration is attributed to the highly confined porosity (pore size: 5.6 Å *vs.* kinetic diameter of acetone: 4.6 Å), combined with its inherent hydrophobic pore characteristics, eliminating the need for additional grafting of organic linkers or external surface coating. Guided by these computational predictions, we optimized CAU-11's synthesis and rigorously evaluated its adsorption properties. Single-component water adsorption measurements confirmed the exceptional hydrophobicity of CAU-11(Al), a feature rarely observed among MOF materials. Complementary MC-*NVT* simulations shed light on the underlying water adsorption mechanism, helping to rationalize this remarkable behavior. Advanced sorption measurements revealed excellent low-pressure acetone uptakes, while gas-phase pulse chromatography evidenced high Henry's law constants (K_H) and adsorption enthalpies ($\Delta H_{ads,0}$). Beyond confirming the highly attractive capture performance of CAU-11(Al), these experimental data further served to refine the FF parameters for a more accurate description of the MOF/acetone interactions. Ravichandran *et al.*[47] evidenced earlier that importance sampling (IS) is an effective strategy to refine the framework force field parameters to achieve a better agreement between simulated and experimental adsorption isotherms for ZIF-8 and ethane/ethylene in the low-pressure regime. We applied this strategy to the CAU-11(Al)/acetone system to gain a precise microscopic description of the acetone adsorption mechanism in the low-pressure range. Decisively, binary water/acetone mixture breakthrough experiments combined with GCMC simulations demonstrated an unprecedented level of selective acetone capture under humidity with only minimal decrease in acetone adsorption capacity compared to dry environment.

2 Methodology

2.1 MOFs selection and geometrical/textural analysis

A selection of MOFs featuring distinct pore dimension/shape, various fluorine-based functionalities decorating the ligands, typical hydrophobic/hydrophilic balance and different metal centers were examined. This list includes: CAU-8-bpdc(Al), CAU-8-odb(Al), CAU-10-H(Al), CAU-10-CH_3(Al), CAU-10-OCH_3(Al), CAU-11(Al), CAU-21-odb(Al), CAU-21-bpdc(Al), Ce-RPF-4, MIL-53-ndc(Al), MIL-53-CF_3(Al), MIL-53-F_4(Al) and Al-Fum. These MOFs possess pore sizes suitable for acetone adsorption (*i.e.*, pore size larger than the kinetic diameter of acetone 4.6 Å) ranging from 4.7 Å to 6.9 Å to explore distinct degree of confinement for acetone, and/or pore surfaces decorated by functionalities that can favor *a priori* preferential interactions towards acetone. Zeo++ software was used for the geometrical–textural analysis of the considered MOFs, including largest cavity diameter (LCD), pore limiting diameter (PLD), density, accessible probe-occupiable volume (POAV), and void fraction (φ).[48,49] Complete structural details, compositions, and computed properties of MOFs are provided in ESI Section S1.†

2.2 Periodic DFT calculations

All the MOF structures were fully geometry optimized, (*i.e.*, both atomic positions and cell parameters), at the DFT-level using the Vienna *Ab Initio* Simulation Package (VASP) version 6.4 (ref. 50–52) employing a widely adopted level of theory routinely applied in previous studies.[15,53] The Perdew–Burke–Ernzerhof (PBE) exchange–correlation functional was used in combination of Grimme's D3 dispersion correction with Becke–Johnson damping.[54–56] The core and valence electrons of the interacting atoms were treated with projector-augmented-wave (PAW) potentials[57] and plane-wave basis sets, respectively. A plane wave kinetic energy cutoff of 800 eV and gamma point meshes for sampling the Brillouin zone were used. The convergence criteria were set to 0.01 eV $Å^{-1}$ for the forces and 10^{-6} eV for the electronic energy. The same strategy was applied to optimize all MOFs loaded with 1 acetone molecule per unit cell. The converged electronic densities of the empty MOFs were used to derive atomic partial charges for the structures using density-derived electrostatic and chemical (DDEC) charge partitioning scheme as implemented in the Chargemol software.[58–61]

The interaction energies (E_{int}) between acetone or water and this series of MOFs were further computed as: $E_{\text{int}} = E_{\text{MOF+guest}} - (E_{\text{MOF}} + E_{\text{guest}})$; where $E_{\text{MOF+guest}}$ is the electronic ground state energy of the fully optimized MOF/guest system, with one acetone or water molecule per unit cell, while E_{MOF} and E_{guest} correspond to the ground state energies of an empty MOF and an isolated acetone or water molecule, respectively.

2.3 Monte Carlo simulations

Acetone and water affinities of the DFT-optimized MOF materials were assessed based on the $\Delta H_{\text{ads},0}$ and K_{H} calculated at infinite dilution using Widom's test particle insertion method.[62] For these calculations, 1×10^6 and 2×10^6 cycles were used for equilibration and production stages, respectively. The adsorption uptake of all these MOFs were assessed at very low acetone pressure, *i.e.* 1 Pa (10 ppm), using grand canonical Monte Carlo simulations (GCMC). For the top-performing material, CAU-11(Al), the full acetone adsorption isotherm was computed at 298 K up to a relative pressure of $P/P_0 = 0.1$ (3050 Pa, or 30 500 ppm; see Tables S6 and S7†). MC simulations in the *NVT* ensemble were performed for CAU-11(Al) loaded with a single water molecule per simulation box as well as three different water loadings, selected to cover low, moderate and high-water sorption uptakes measured experimentally: 15.2, 30.1, and 56.2 $cm^3\ g^{-1}$ (at $P/P_0 = 0.57$, 0.80 and 0.90), corresponding to 1, 2, and 4 molecules per unit cell, respectively. Binary acetone/water mixture GCMC simulations for a fixed water content of 40% RH were carried out up to $P/P_0 = 0.1$ for acetone partial pressure (see Table S8†). For each pressure point in both single-component and binary mixture GCMC, and MC-*NVT* simulations, 1×10^8 MC steps for equilibration and 2×10^8 MC steps were used for production runs. All these calculations were conducted with the Complex Adsorption and Diffusion Simulation Suite (CADSS) code.[63] Intermolecular interactions between the framework atoms and both acetone and water atoms were described by a combination of site-to-site Lennard-Jones (LJ) and coulombic contributions. DREIDING and UFF force field parameters were adopted to describe the LJ parameters of the atoms of the inorganic and organic units of the MOFs,[64,65] respectively, while DFT derived DDEC atomic partial charges were employed to account for coulombic contributions. Additionally, the LJ parameter, ε for hydrogen of the μ-OH groups and for metal ions of the MOFs were turned off, allowing these atoms to interact with adsorbate molecules only through electrostatic interactions (see ESI Table S2† for the list of LJ parameters considered for all MOF atoms). This strategy has been previously reported as effective to accurately describe the adsorption properties of MOFs for polar molecules such as water.[66–68] Short-range dispersion forces were truncated at a cutoff radius of 12 Å while the interactions between unlike FF centers were treated by means of the Lorentz–Berthelot combination rule. The long-range electrostatic interactions were handled using the Ewald summation technique. Water molecule was modelled using the TIP4P/2005 (ref. 69) model, while acetone molecule was treated with the united atom approach in the TraPPE[70] FF (see ESI, Table S3† for the list of LJ parameters for adsorbate molecules).

To evaluate the selective acetone adsorption performance of the MOFs, two metrics were considered: the ideal selectivity (S_{ideal}) and the performance factor (P). The ideal selectivity is defined as the ratio of K_{H} for acetone and for water at infinite dilution:

$$S_{\text{ideal}} = \frac{K_{\text{H(acetone)}}}{K_{\text{H(water)}}}$$

Another adsorption performance factor, labeled as P, was calculated for all MOFs integrating in addition to their selectivity, their acetone adsorption uptake (Q_{acetone}) at 10 ppm[13,71] as defined below:

$$P = (Q_{\text{acetone},10\ \text{ppm}})\ln S_{\text{ideal}}$$

2.4 Importance sampling

The importance sampling (IS) technique allows for the exploration of the potential energy surface of a MOF/guest system to obtain Henry's law constants and adsorption enthalpies at a quantum level of accuracy.[47,72] The IS methodology was applied to the identified top performing CAU-11(Al) aiming to refine the initial FF parameters of the MOF. The IS method first consisted of conducting a Widom's test particle insertion simulation, generating a set of configurations (typically, 1×10^6) with a single molecule inserted into the MOF pore. From this, a smaller subset of configurations was selected according to the Boltzmann factor, considering the FF-computed energy of each configuration during Widom insertion calculations. For this subset of configurations, *ab initio* E_{int} were computed to derive a correction factor, λ, which corresponds to the difference between the FF-calculated energy, $E_{\text{int}}^{\text{FF}}$, and the *ab initio* $E_{\text{int}}^{\text{DFT}}$ (eqn (1)). The optimized scaling parameter, λ, was then used to obtain corrected values of the Henry's law constant (K_{H}^{IS}) and adsorption enthalpy ($\Delta H_{\text{ads},0}^{\text{IS}}$), as follows:

$$\lambda = \frac{1}{n}\sum_{i=1}^{n} \mathrm{e}^{-\beta\left(E_{\text{int},i}^{\text{DFT}} - E_{\text{int},i}^{\text{FF}}\right)} \tag{1}$$

$$K_{\text{H}}^{\text{IS}} = \lambda \times K_{\text{H}}^{\text{FF}} \tag{2}$$

$$\Delta H_{\text{ads},0}^{\text{IS}} = \frac{\frac{1}{n}\sum_{i=1}^{n} E_{\text{int},i}^{\text{DFT}} \times \mathrm{e}^{-\beta\left(E_{\text{int},i}^{\text{DFT}} - E_{\text{int},i}^{\text{FF}}\right)}}{\lambda} - \frac{1}{\beta} \tag{3}$$

Further details of the methodology and validation in MOFs have been previously reported in literature.[47,72] For this IS procedure, *ab initio* single-point calculations for the selected configurations were conducted in VASP, implementing the same theoretical level described earlier in the Geometry optimization section. To ensure that the chosen number of configurations was adequate to sample the entire potential energy surface, convergence tests for both the K_{H}^{IS} and $\Delta H_{\text{ads},0}^{\text{IS}}$ were performed determining $n = 1000$ for acetone/CAU-11 case (Fig. S6†).

Following an approach described by Ravichandran *et al.*,[47] using the refined K_{H}^{IS} and $\Delta H_{\text{ads},0}^{\text{IS}}$ values, the LJ parameter ε for the MOF atoms were adjusted, and the energy associated to host–guest configurations was computed iteratively until it matched the value predicted by the importance sampling. Finally, these rescaled force field parameters were used to perform GCMC calculations to recalculate the acetone adsorption isotherm to gain a more accurate description in the low-pressure range, using the same GCMC simulation settings described in Section 2.3. The rescaled force field parameters can be found in the ESI (Table S5).†

2.5 Experimental details

2.5.1 Synthesis of CAU-11(Al), [Al(OH)(SDBA)]. Synthesis of CAU-11(Al) was carried out according to the literature.[46] All chemicals are commercially available and were employed without further purification. CAU-11(Al) was prepared by mixing $AlCl_3 \cdot 6H_2O$ (724 mg, 3 mmol), 4,4′-sulfonyldibenzoic acid (H_2SDBA) (268 mg, 1.2 mmol), 2 M aqueous solution of NaOH (1.8 mL, 3.6 mmol), and 18.2 mL water. The mixture was then placed in a 30 mL Teflon-lined steel autoclave lined with Teflon. The reaction was performed under conventional heating at 150 °C for 12 hours, with 1 hour of heating and 1 hour of cooling. The resulting precipitate was filtered off and washed with DMF under microwave heating at 150 °C for 1 hour. After cooling to room temperature, the solid was filtered off and air dried.

2.5.2 Characterization methods. Powder X-ray diffraction data were collected on a STOE Stadi MP instrument equipped with a MYTHEN 1K detector using CuKα1 radiation. Infrared spectra of the compounds were collected using a Bruker ALPHA-FT-IR A220/D-01 with an ATR unit. Thermogravimetric measurements were performed on a Linseis STA PT 1000 (airflow = 6 $\text{dm}^3\ \text{h}^{-1}$, heating rate 8 K min^{-1}). The sample amount was approximately 20 mg. The high-humidity stability test for CAU-11 was conducted by placing 50 mg of the material in a 2 mL Teflon vial, which was then sealed inside a 30 mL Teflon vessel containing 5 mL of water. The setup was heated in an autoclave at 120 °C for 24 hours, after which PXRD analysis was performed.

For the liquid-phase stability tests, 50 mg of CAU-11 were stirred in 5 mL of either water or acetone at room temperature for 24 hours. PXRD patterns were collected after exposure. High-resolution argon (87 K) adsorption isotherm was measured using a manometric sorption analyser, equipped with 1, 10, and 1000 Torr transducers (Autosorb iQ MP, Anton-Paar, Quantatec, Boynton Beach, FL) over a wide range of relative pressures (P/P_0) from 10^{-6} to 1.0. Surface area and pore size analysis were obtained by analysing the high-resolution argon isotherm by the BET method and by applying a dedicated NLDFT (non-local-density-functional theory) method on the adsorption data, assuming an oxidic surface and cylindrical pore geometry. Further details and characterization results can be found in Section S3 in the ESI.†

2.5.3 Adsorption measurements. Adsorption measurements were collected over a relative pressure range from 0.0006 to 0.99 for acetone and 0.006 and 0.99 for water at 25 °C using a dedicated manometric vapor sorption analyser (Vstar, Anton Paar QuantaTec, Boynton Beach, FL, USA). The whole system (with exception of the separately temperature controlled sample cell environment) was kept at 100 °C (for eliminating any cold spots on which wetting/condensation of vapours could occur) for accurate vapour sorption experiments. Prior to the adsorption experiments the samples were degassed at 200 °C for 12 hours under vacuum. For acetone, two consecutive adsorption–desorption measurement runs were performed in the same aliquot with the sample being re-outgassed at 200 °C before starting the second run.

2.5.4 Gas-phase pulse chromatography. Acetone adsorption at very low concentration (Henry regime) was assessed using a customized inverse gas chromatography instrument developed in-house, based on an Agilent Technologies 7820A gas chromatograph. Acetone detection was accomplished using a flame ionization detector. A stainless-steel column (length = 10 cm and inner diameter = 0.216 cm) was filled with adsorbent pellets to minimize pressure drop within the column. Pelletization of the CAU-11(Al) powder was accomplished by compressing adsorbent powder using a mechanical press, followed by crushing and sieving to pellets sized between 400 and 600 μm. Before conducting pulse IGC experiments, the MOF-containing column underwent activation at 200 °C for 16 hours under a helium flow. A small pulse (0.01 μL) of acetone was injected using an auto injector. Helium served as the carrier gas at a flow rate of 30 NmL min^{-1}. The dead time was quantified using a zero-volume connecter in absence of a column, and the obtained values were subtracted from the first-order moment. Three repetitions were performed, and the mean value was utilized for the calculations. The Henry's law constant was determined through the first order moment of chromatograms, while adsorption enthalpies were derived from the temperature dependence of the K_H, utilizing the Van't Hoff equation.

2.5.5 Breakthrough curves. Vapor phase breakthrough experiments with acetone were conducted under both dry and humid conditions to evaluate the impact of water on acetone adsorption at low acetone concentration, using an in-house build setup.[73] In these experiments, two separate streams of helium carrier gas pass through bubbler evaporators containing acetone or water respectively. The vapor pressure of water and acetone is controlled by adjusting the temperature of the bubbler evaporators. The produced acetone and water containing streams are subsequently combined and may be further diluted with the use of a third mass flow controller to adjust the final partial pressures. The (un)diluted vapors are routed either to an adsorption column packed with CAU-11(Al) pellets, maintained at a constant temperature, or they bypass the column entirely. The stream eluting at the column outlet is analyzed through periodic sampling of the gas stream, followed by automated injection into a gas chromatograph (HP-6890). The GC used for the analysis contained a 0.25 mm i.d. Stabilwax® column (Restek) and was equipped with a Thermal Conductivity Detector (TCD), employing He as the carrier gas. Following each breakthrough experiment, the adsorption column undergoes regeneration by purging with carrier and heating the column in the oven at a 1 °C min^{-1} to 200 °C and maintaining this final temperature for 180 min. All extra-column tubing was heated to inhibit vapor condensation within the apparatus.

3 Results and discussion

3.1 Predicted acetone adsorption performance of MOFs

The acetone affinity of all explored MOFs was evaluated on the basis of K_H and $\Delta H_{\text{ads},0}$ values calculated at infinite dilution. All the investigated MOFs exhibit $\Delta H_{\text{ads},0}$ exceeding the vaporization enthalpy of acetone at 298 K (32 kJ mol^{-1})[74] (Fig. 1a) emphasizing that acetone adsorption is favorable in this full set of MOFs. Additionally, we computed the interaction energy for acetone in all these MOFs *via* periodic DFT calculations. Notably, the force field-derived $\Delta H_{\text{ads},0}$ at 298 K exhibits a trend consistent with the DFT-calculated acetone–MOF interaction energies (Fig. 1b) indicating that the selected force field provides a sufficiently accurate foundation for an initial, reliable assessment of MOF performance ranking. The DFT-optimized acetone loaded structures were also analyzed and their characteristic host/guest interacting distances (Fig. S1, S2,† and 1c, top) associated to the preferential arrangement of acetone in the pores were compared with the radial distribution functions (RDFs) averaged over the configurations generated by GCMC simulations performed for acetone uptake at 10 ppm (Fig. S1, S2,† and 1c, bottom). The maximum intensity of the RDFs plotted for the most representative MOF/acetone atom pairs is in qualitative agreement with the corresponding distance observed in the DFT-optimized structures. This observation emphasizes that the FF-GCMC simulations enable to deliver valuable molecular-level insight into the adsorption behavior of acetone within these materials.

MOFs with pore diameters close to the kinetic diameter of acetone (4.6 Å) and low pore volumes (V_p), such as CAU-21-odb(Al) (LCD: 5.3 Å, V_p: 0.13 $\text{cm}^3\ \text{g}^{-1}$), MIL-53-$F_4$(Al) (LCD: 4.7 Å, V_p: 0.14 $\text{cm}^3\ \text{g}^{-1}$), and Ce-RPF-4 (LCD: 5.1 Å, V_p: 0.11 $\text{cm}^3\ \text{g}^{-1}$), exhibit the strongest acetone affinities as revealed by their three highest $\Delta H_{\text{ads},0}$ values of −66.3, −65.3 and −62.6 kJ mol^{-1}, respectively. In contrast, MIL-53-ndc(Al), with the largest pore size and highest occupiable volume (LCD: 6.8 Å, V_p: 0.42 $\text{cm}^3\ \text{g}^{-1}$), displays the least favorable $\Delta H_{\text{ads},0}$ of −41.3 kJ mol^{-1} (Fig. 1a). Optimal acetone packing within fine-tuned pores highlights the crucial role of confinement in the strong acetone affinity of these MOF frameworks. The confinement effect is further highlighted in the Ce-RPF-4 MOF, which features three distinct cavity sizes within its pore topology. A careful inspection of the GCMC adsorption configurations suggests that acetone molecules preferentially occupy the smaller square-shaped channel. This is corroborated by shorter characteristic separating distances in the RDF profiles for the acetone and MOF atoms in this channel (*viz.*, $\text{H}\cdots\text{O}_{\text{acetone}}$), compared to those involving fluorine atoms associated to CF_3 groups pointing into the larger hexagonal pore. Notably, a significant RDF peak for $\text{F}\cdots\text{O}_{\text{acetone}}$ appears only at 4 Å (Fig. 1c). This trend persists across the bi-modal CAU-8 series, where acetone selectively occupies more confined cavities at low loadings (Fig. S2†). Similarly, in the isoreticular CAU-10 series, higher $\Delta H_{\text{ads},0}$ are calculated for MOFs with smaller pore size/volume, such as CAU-10-CH_3(Al) (LCD: 5.9 Å, V_p: 0.14 $\text{cm}^3\ \text{g}^{-1}$) and CAU-10-0$CH_3$(Al) (LCD: 5.8 Å, V_p: 0.09 $\text{cm}^3\ \text{g}^{-1}$), compared to CAU-10-H(Al) (LCD: 6.0 Å, V_p: 0.18 $\text{cm}^3\ \text{g}^{-1}$).

Alongside confinement, the presence of specific adsorption sites in the MOF pore wall also increases acetone affinity as typically illustrated in the DFT-optimized acetone geometries of CAU-21(Al) and MIL-53-F_4(Al), and related RDFs obtained by MC simulations (Fig. 1c). As a general trend, the closest MOF⋯acetone atom contacts occur with the oxygen atom of acetone and its $-CH_3$ group is positioned farther from the framework atoms, and does not engage in significant interactions with the MOF (Fig. S3†). CAU-21-odb(Al) and MIL-53-F_4(Al) not only have pore sizes tailored for an optimal packing of acetone but also feature μ-OH groups bridging Al atoms in their inorganic units. Both FF-based simulations and DFT calculations predict that acetone molecules preferentially orient their oxygen atoms toward the hydrogen atoms of these μ-OH groups, forming short hydrogen bonds—2.08 Å in CAU-21-odb(Al) and 1.74 Å in the more confined MIL-53-F_4(Al). This strong acetone/MOF

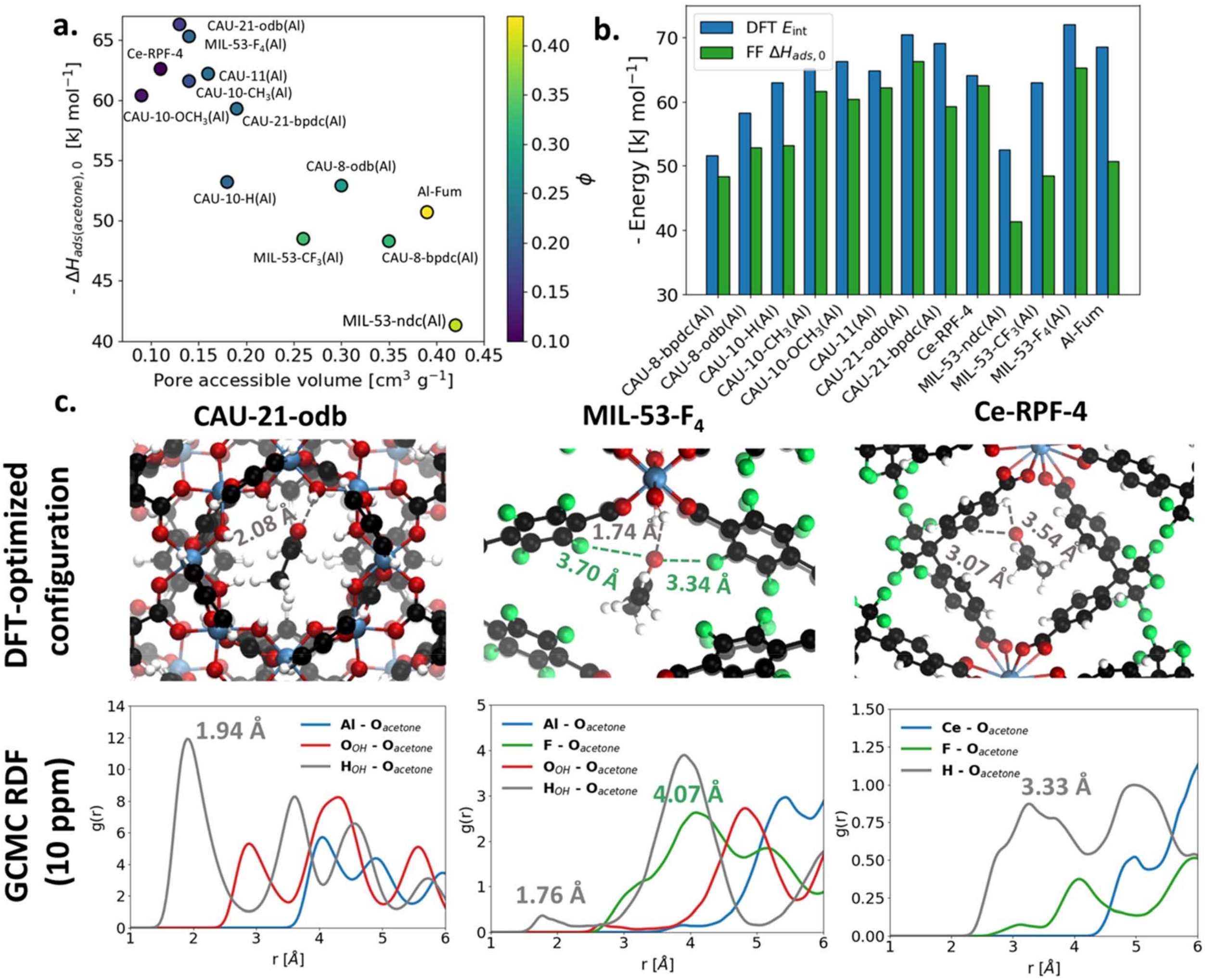

Fig. 1 (a) Relationship between the simulated $\Delta H_{ads,0}$ at infinite dilution using Widom insertion method for acetone at 298 K and the respective accessible pore volume and void fraction of the considered MOFs; (b) comparison of DFT-calculated interaction energy and simulated $\Delta H_{ads,0}$ at 298 K for acetone; (c) on the top, DFT optimized configurations for the top three MOFs with the highest acetone affinities, showing the shortest acetone–MOF interacting distances; on the bottom, the corresponding RDF profiles for the most representative MOF/acetone atom pairs averaged over the GCMC configurations generated at 10 ppm.

interaction enhances acetone affinity in complement to the high confinement. The comparison between CAU-21-odb(Al) and Ce-RPF-4 further highlights the influence of adsorption sites. Although Ce-RPF-4 has more confined pores, CAU-21-odb(Al) exhibits 4 kJ mol^{-1} higher $\Delta H_{ads,0}$, reinforcing the significance of hydrogen bonding interactions in acetone adsorption. Conversely, despite sharing the same topology as CAU-21-odb(Al) and containing μ-OH groups, CAU-21-bpdc(Al) presents a lower $\Delta H_{ads,0}$ of −59 kJ mol^{-1} due to its larger pore size (LCD: 6.9 Å, V_p: 0.19 cm^3 g^{-1}), emphasizing the role of confinement in adsorption energetics.

When analyzing the GCMC-simulated acetone adsorption uptake at 10 ppm, it becomes clear that MOF frameworks where acetone molecules are less confined, such as MIL-53-ndc(Al) and both CAU-8 MOFs variants, exhibit very low acetone loadings in this very low-pressure range. Additionally, steric hindrance from bulky groups like –OCH$_3$, –CF$_3$, and the 4-fluoro-substituted benzene-carboxylate linker in CAU-10-OCH$_3$(Al), MIL-53-CF$_3$(Al), and MIL-53-F$_4$(Al), respectively, results in low sorption uptakes (Table S4†). Notably, CAU-11(Al) and CAU-10-CH$_3$(Al) are predicted as the MOFs with the highest acetone capacities at 10 ppm (Table S4†).

3.2 Predicted selective acetone over water adsorption performance of MOFs

Potential interference from atmospheric humidity is a common challenge in real-world applications especially for the selective capture of acetone in indoor air. The selective adsorption ability of the distinct MOFs was first assessed by means of the ideal selectivity (S_{ideal}) that can be calculated as the ratio of K_H for acetone and for water. We used this metrics along alongside the performance factor (P) that incorporates also the acetone uptake simulated at a concentration of 10 ppm, to qualitatively rank the MOFs studied in this study (Fig. 2 and Table S4†).

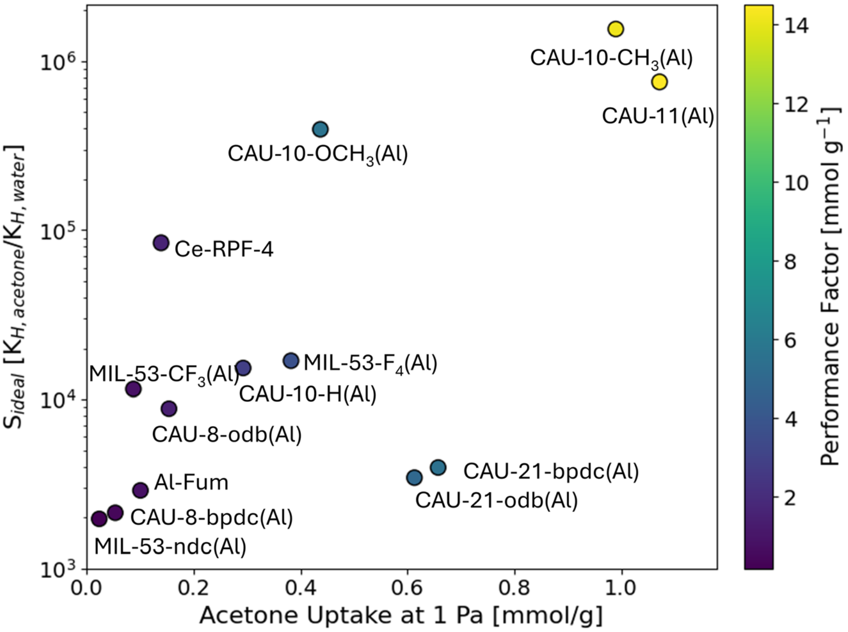

Fig. 2 Plot of the calculated ideal selectivity (S_{ideal}) of acetone/water *vs.* the simulated acetone uptake at trace concentrations (1 Pa = 10 ppm, 298 K). Data points are color-mapped to the performance factor ($P = Q_{\text{acetone,10 ppm}} \ln S_{\text{ideal}}$) calculated for all MOFs. High-performing MOFs (top-right quadrant, colored yellow) simultaneously achieve high selective acetone adsorption against water vapor and high acetone uptake at very low concentration.

Considering the K_H value calculated for the benchmark hydrophobic adsorbent ZIF-8,[75] we have identified five highly hydrophobic MOFs: CAU-11(Al), CAU-10-CH$_3$(Al), CAU-10-OCH$_3$(Al), Ce-RPF-4 and MIL-53-CF$_3$(Al) possessing $K_{\text{H(water)}}$ on the order of 10^{-6} mol kg^{-1} Pa^{-1}. These MOFs share a common feature—hydrophobic linkers containing alkyl, aryl, or fluorinated groups. In contrast, although CAU-21-odb(Al) and MIL-53-F$_4$(Al) are identified as high-affinity materials for acetone, they are also the most hydrophilic among the considered MOFs with $K_{\text{H(water)}}$ values around 10^{-4} mol kg^{-1} Pa^{-1}. The presence of μ-OH groups makes these materials more susceptible to water adsorption, resulting in poor selectivity for the adsorption of acetone over water compared to the other more hydrophobic MOFs.

Fig. 2 shows that CAU-10-CH$_3$(Al) and CAU-11(Al) exhibit outstanding acetone selectivity over water and the highest values for *P*. Overall, CAU-11(Al) stands out as the top-performing candidate due to its strong acetone affinity, remarkable hydrophobicity, and superior acetone adsorption capacity among all MOF materials considered. These observations suggest that, for the effective capture of polar volatile organic compounds like acetone a finely-tuned pore structure for molecular confinement, combined with a hydrophobic linker, are crucial factors to consider. This aligns with the observations made by Severino *et al.*,[33] who found that the inclusion of a hydrophobic –CF$_3$ group in MIL-53(Al) enhances the capture of the polar molecule acetic acid.

3.3 Unravelling the hydrophobicity of the best candidate CAU-11(Al)

DFT calculations performed for CAU-11(Al) loaded with a single water molecule supported the conclusions gained from the Widom's insertion method, demonstrating a rather low E_{int} of −36.6 kJ mol^{-1}. MC-*NVT* simulations with a single water molecule per simulation box equally revealed no directional or site-specific interactions, underscoring the low water affinity of CAU-11(Al) (Fig. S4†). To confirm the predicted hydrophobicity of CAU-11(Al), the MOF sample was synthesized following the previously reported procedure.[46] The resulting PXRD pattern confirmed phase purity (also supported by the elemental chemical analysis provided in Table S10†) and matched well with the simulated structure (Fig. S7†) while its IR spectra (Fig. S8 and Table S9†), Scanning Electron Microscopy (SEM) images (Fig. S9†) and TGA profiles (Fig. S10†) are consistent with the previously reported data.[46] Further textural characterization of the CAU-11(Al) sample was performed using an argon adsorption isotherm at 87 K (Fig. S11†). An apparent BET surface area of 357 m^2 g^{-1} was obtained by applying the criteria recommended by Rouquerol *et al.*[76,77] for selecting the linear BET region. NLDFT analysis revealed a narrow pore size distribution centered at 0.55 nm and a micropore volume of 0.17 cm^3 g^{-1} (Fig. S11†), in alignment with the simulated geometric values of 5.6 Å and 0.16 cm^3 g^{-1} (Table S1†). Interestingly the material initially exposed to high humidity levels, at 120 °C for 24 hours, was demonstrated to maintain the same PXRD patterns than the pristine material (Fig. S7b†), highlighting its good stability upon water vapor sorption.

Single-component water adsorption isotherm was then collected for this sample. On the contrary of argon that leads to type I-isotherms with a pore filling at low relative pressures ($P/P_0 < 0.1$) (Fig. S12†), water micropore filling is shifted to very high relative pressures ($P/P_0 > 0.9$), clearly indicating a very high hydrophobicity of CAU-11(Al) (Fig. 3a). One observes that the

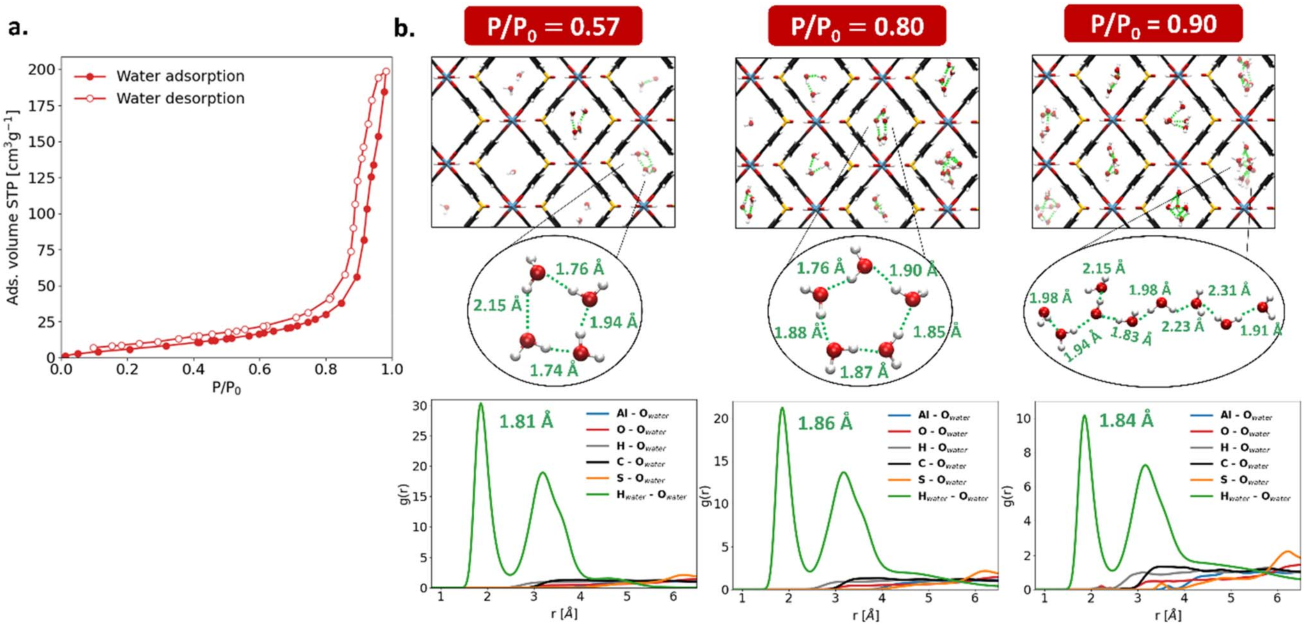

Fig. 3 Water adsorption in CAU-11(Al). (a) Single-component adsorption isotherm at 25 °C for CAU-11(Al); (b) water adsorption mechanism in CAU-11(Al) at different partial pressures depicted with representative configurations from MC-*NVT* simulations and associated RDFs for the MOF/water atom pairs. In the *NVT* snapshots, the H-bonds between the oxygen and hydrogen atoms from water are displayed in green, and were computed using geometric criteria of O–H···O (donor-H···acceptor) distance < 2.5 Å and O–H···O angle > 120°.

water sorption is accompanied by an intrinsic hysteresis loop most likely associated with the existence of long-lived metastable states of adsorbed water clusters, as observed in other micro–mesoporous materials.[78,79] MC-*NVT* simulations, using water loadings corresponding to experimental uptakes obtained experimentally at relative partial pressures before and after the isotherm inflection point, shed light on the water adsorption mechanism. We revealed that water molecules interact only weakly with the MOF pore wall and rather preferentially form hydrogen-bonded water clusters with typical H-bond distances ranging between 1.81 and 1.86 Å (Fig. 3b and S5†). Even at very low loading ($P/P_0 = 0.57$; 15.2 $cm^3\ g^{-1}$), there is already a clear tendency for water molecules to form clusters. Despite the low concentration, water prefers to associate into dimers or cyclic tetramers, with isolated molecules rarely found within the pores. As the isotherm rises ($P/P_0 = 0.8$), the number of adsorbed molecules increases, favoring the formation of cyclic trimers and pentamers. At higher loading (56.2 $cm^3\ g^{-1}$; $P/P_0 = 0.9$), water clustering occurs within the MOF channels, forming discrete clusters of up to 8 to 12 molecules. Notably, these adsorbed water networks maintain an average of approximately two hydrogen bonds per molecule under all simulated conditions, a significantly lower coordination than in bulk liquid water (~3.6 H-bonds), reflecting the constrained hydrogen-bonding environment within the hydrophobic pores of CAU-11(Al).

Furthermore, from the experimental water adsorption isotherm, very low hydrophilicity index of 0.19 was estimated by applying the concept of hydrophilicity/hydrophobicity index (larger the deviation from 1, greater the surface hydrophobicity).[80] These observations emphasize that at typical indoor humidities (RH: 30–60%) the water uptake is ideally minimal.

3.4 In-depth exploration of the single-component acetone adsorption in the best predicted MOF CAU-11(Al)

To confirm the promising predicted acetone capture properties of CAU-11(Al), experimental single-component adsorption isotherms were then collected and compared with the corresponding GCMC-simulated data. Overall, a good agreement was observed between the experimental and simulated results (Fig. 4a), with acetone uptakes of 1.96 mmol g^{-1} and 1.99 mmol g^{-1} at $P \approx 3050$ Pa for experimental and simulated results, respectively. However, a deviation can be noted particularly in the very low-pressure regime, $P \leq 1000$ Pa (see inset Fig. 4a). K_H of acetone was also determined *via* gas-phase pulse chromatography using the first-order moment of chromatograms, yielding a value of 0.55 mol kg^{-1} mol^{-1}. Adsorption enthalpies derived from the temperature dependence of the K_H, utilizing the Van't Hoff equation resulted in −55.4 kJ mol^{-1} (Fig. 4b), further confirming the strong affinity between acetone and CAU-11(Al). Comparing these experimental values with the FF-based Widom insertion predicted results ($\Delta H_{ads,0} = -62.2$ kJ mol^{-1}, $K_H = 4.15$ mol kg^{-1} Pa^{-1}), we confirmed that the overestimation in the simulated adsorption isotherm at low-coverage regime aligns with the higher affinity predicted by our simulations.

We further adopted the IS strategy to fine tune the force field parameters to describe the interactions between acetone and the CAU-11(Al) framework. This rescaling procedure involved iteratively adjusting the LJ ε value only for the framework atoms in the original UFF/DREIDING FF used for the Widom insertion calculations until the $\Delta H_{ads,0}/K_H$ reached the values computed *via* the IS method, ultimately converging towards the experimental data.

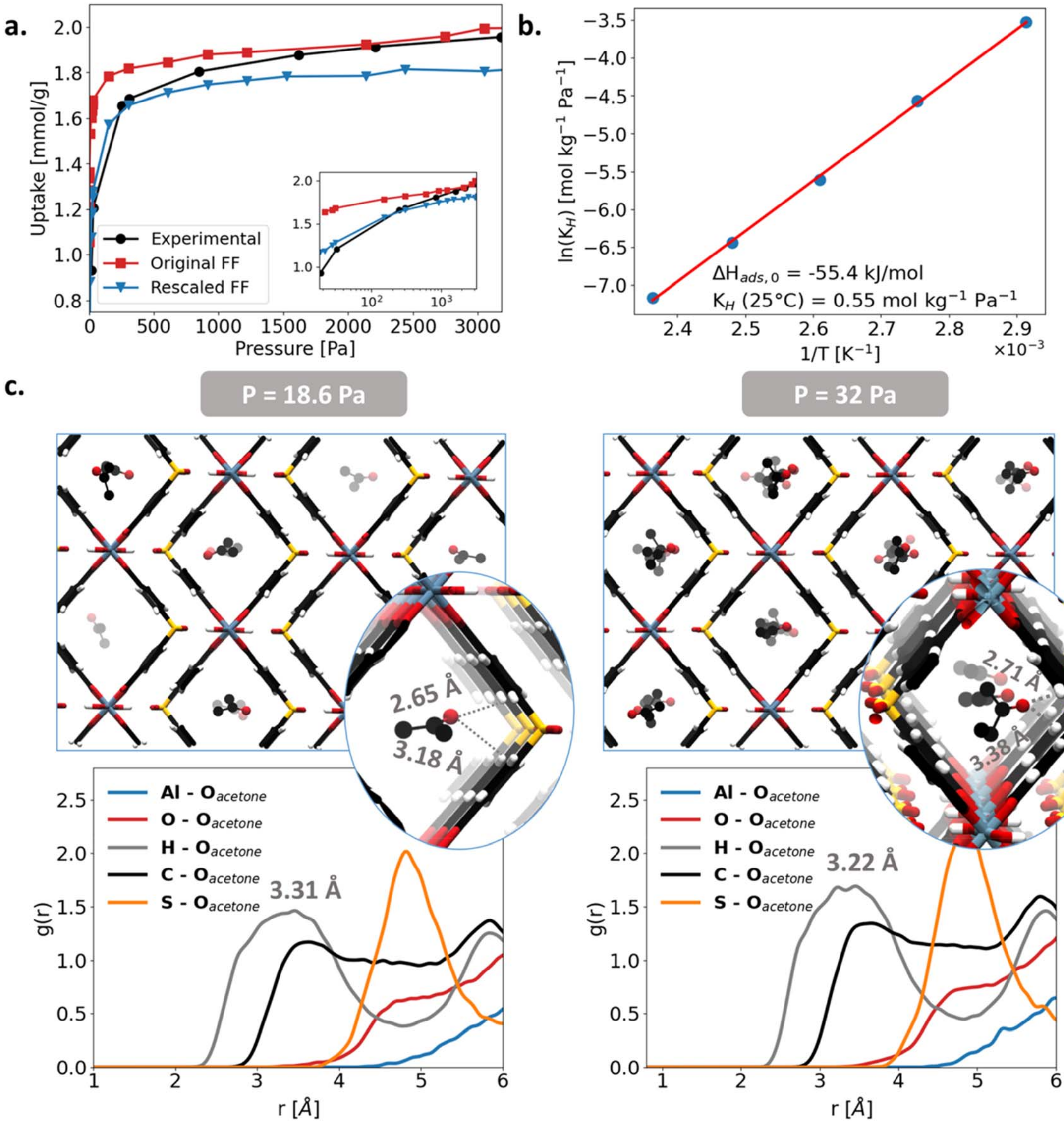

Fig. 4 Single-component acetone adsorption in CAU-11(Al). (a) Acetone adsorption isotherms from adsorption measurements (black circles), GCMC simulations with original MOF force-field parameters (red squares) and GCMC simulations with rescaled force-field parameters (blue triangles); (b) Van't Hoff plot for acetone adsorption in CAU-11(Al) along the calculated $\Delta H_{\mathrm{ads},0}$ and extrapolated K_H at 25 °C; (c) microscopic adsorption mechanism of acetone molecules in CAU-11(Al) depicted with representative GCMC configurations and associated RDFs for the MOF/acetone atom pairs derived from the rescaled FF simulations at $P = 18.6$ Pa (186 ppm) and $P = 32$ Pa (320 ppm).

Table 1 shows that $\Delta H_{\mathrm{ads},0}$ and K_{H} obtained *via* IS method exhibits excellent agreement with experimental data when applying a rescaling of 0.76ε to all the original MOF atom force field parameters. This refinement also significantly improved the correspondence with the experimental adsorption isotherm in the low-pressure range, as depicted in Fig. 4a. The rescaled FF parameters are provided in the ESI, Table S5.†

Notably, as shown in Fig. 4a, the adjustment of the LJ ε parameter of the MOF atoms mostly affects the GCMC simulations data at low pressures, while its effect is minimal at higher pressures (see Tables S6 and S7† for the acetone uptakes). Notably, the very first collected experimental data point at an acetone concentration of 186 ppm reveals an uptake of 0.93 mmol g^{-1} *vs.* 1.62 mmol g^{-1} (original FF) and 1.17 mmol g^{-1} (rescaled FF). The rescaled FF-GCMC simulations lead to a predicted acetone uptake at 320 ppm (1.21 mmol g^{-1}) in excellent agreement with the experimental value (1.28 mmol g^{-1}).

Fig. 4c evidences that at 186 ppm, acetone molecules are mainly located in the center of the channel in line with the DFT-optimized geometry of 1 acetone molecule in this MOF (Fig. S1†), the acetone molecules having their oxygen atoms positioned closer to the hydrogen atoms of the SDBA linkers, with H_{SDBA}–O_{acetone} distance starting as low as 2.4 Å as revealed by the corresponding RDF plot. This scenario holds also true at a higher acetone concentration as equally illustrated in Fig. 4c.

Finally, two consecutive acetone adsorption–desorption sorption experiments were performed on the same sample, showing essentially perfect reproducibility between cycles

Table 1 Adsorption enthalpies and Henry's law constants simulated by force field-based Widom insertion calculations and the importance sampling method alongside the comparison with experimental data obtained from gas-phase pulse chromatography measurements

	$\Delta H_{\text{ads,0(acetone)}}$ [kJ mol^{-1}]	$K_{\text{H(acetone)}}$ [mol kg^{-1} Pa^{-1}]
Original FF simulation	−62.2	4.15
Importance sampling	−54.5	1.79
Gas-phase pulse chromatography	−55.4	0.55

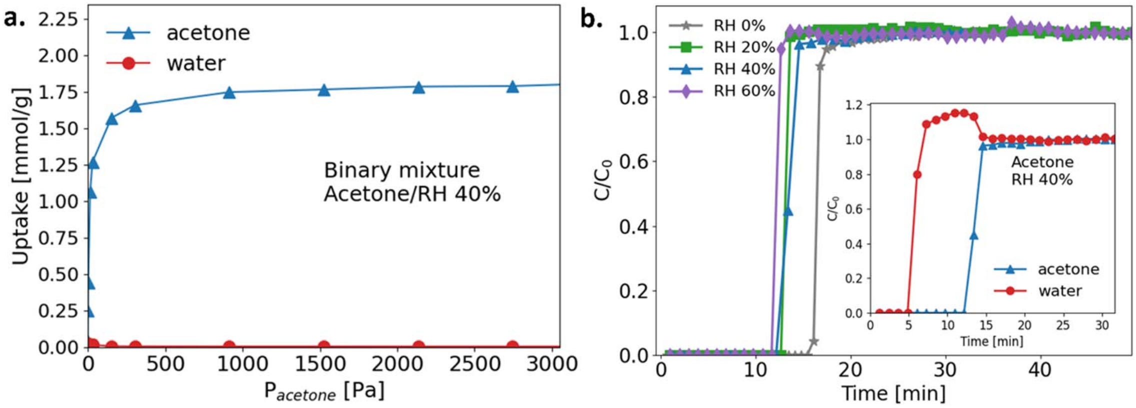

Fig. 5 (a) GCMC-simulated binary adsorption isotherms of acetone and water in CAU-11(Al) at 25 °C. Water partial pressure (P_{H_2O}) was fixed at $0.4P_{H_2O,\text{sat}}$, while acetone partial pressure (P_{acetone}) was varied, considering total pressure of the system, $P_{\text{total}} = P_{\text{acetone}} + P_{H_2O}$. Adsorbed amounts are plotted against P_{acetone}; (b) breakthrough curves under varying relative humidities at 30 °C, along with detailed profiles of acetone and water breakthrough at 40% relative humidity.

(Fig. S13†). These complementary experiments confirmed (i) the good reversibility of acetone adsorption/desorption and (ii) the structural stability of CAU-11(Al) throughout the sorption process.

3.5 Experimental exploration of the selective acetone adsorption over water performance of CAU-11(Al)

The competitive water and acetone adsorption was first explored by GCMC simulations on binary acetone/water mixtures under a constant 40% RH, a common indoor air condition. These calculations revealed that the presence of water does not interfere with acetone adsorption, showing only minimal water uptake (Fig. 5a and Table S8†), while maintaining the acetone saturation capacity obtained from the simulated single-component simulations at 1.81 mmol g^{-1} (Fig. 4a *vs.* 5a). This prediction was decisively confirmed by breakthrough experiments: under humid conditions, the acetone adsorption capacity decreased only marginally, from 0.12 g g^{-1} to 0.10 g g^{-1}, remaining nearly constant across all relative humidities (Fig. 5b and S14†). The acetone uptake measured in the breakthrough experiment under dry conditions (at a partial pressure of 2100 Pa) is consistent with the isotherm results (Fig. 4a and 5b). These results demonstrate that humidity has no significant adverse effect on acetone uptake. The breakthrough time for acetone in dry conditions was 16.7 minutes, which decreased to approximately 13 minutes in humid conditions across all relative humidity levels. Inset of Fig. 5b and S14† report the breakthrough profiles for acetone/water vapor mixture across different RH (0%, 20%, 40% and 60%). We can consistently observe that water elutes first; the small amount of adsorbed water is subsequently displaced by acetone, leading to 'roll-up' of the water concentration profile, confirming its weaker adsorption as compared to acetone.

4 Conclusions

Force field Monte Carlo and density functional theory simulations were initially conducted to predict the acetone affinity of a series of MOFs featuring different hydrophobic organic ligands, pore sizes suitable for acetone confinement and favourable adsorption sites. These calculations revealed that both pore confinement and the presence of specific adsorption sites play a pivotal role to achieve an optimal acetone capture at trace concentrations. The selective acetone capture over water was also predicted for this overall set of MOFs revealing CAU-11(Al) as a stand-out adsorbent. This highly hydrophobic MOF combines high acetone uptake at trace concentrations with excellent acetone/water selectivity owing to an ideal match between its pore dimensions and the molecular size of acetone. These computational predictions were subsequently confirmed through adsorption experiments and gas-phase pulse chromatography, both of which demonstrated strong acetone affinity and significant uptake under low-pressure conditions. Water vapor adsorption isotherms further validated the exceptional hydrophobicity of CAU-11(Al), with water uptake observed only above 85% RH. Most notably, dynamic breakthrough experiments revealed that the presence of water vapor does not compromise acetone adsorption, highlighting the remarkable separation performance of CAU-11(Al) under humid conditions. Altogether, this study highlights CAU-11(Al) as a highly promising material for the selective removal of acetone from humid indoor air, offering a compelling solution to a long-standing challenge in air purification.

Data availability

The data supporting this article have been included as part of the ESI.† The CIF files for the optimized considered initial set of MOFs as well as the experimental adsorption information in AIF file format are available at **https://github.com/sabrinagri/supporting-info**.

Author contributions

S. G. conducted the simulation work; K. K. performed the gas-pulse chromatography and breakthrough curves experiments; I. M. collected the adsorption data; A. P. synthesized and characterized the CAU-11(Al) samples; S. R. provided the required expertise to employ the importance sampling method; G. M., M. W., L. V. and V. V. S. supervised the computational work, J. F. M. D. the breakthrough experiments, M. T. the adsorption measurements and N. S., the synthesis and characterization of the materials.

Conflicts of interest

There are no conflicts to declare.

Acknowledgements

This research work was funded by 101072845 – SENNET (Porous Networks for Gas Sensing) – HORIZON-MSCA-2021-DN-01. The computational work was performed using HPC resources from GENCI-CINES (grant A0180907613). G. M. thanks Institut Universitaire de France for the Senior Chair.

Notes and references

1 S. Dimitroulopoulou, M. R. Dudzińska, L. Gunnarsen, L. Hägerhed, H. Maula, R. Singh, O. Toyinbo and U. Haverinen-Shaughnessy, *Environ. Int.*, 2023, **178**, 108127.
2 J.-L. Mai, W.-W. Yang, Y. Zeng, Y.-F. Guan and S.-J. Chen, *Hyg. Environ. Health Adv.*, 2024, **9**, 100087.
3 B. Siu, A. R. Chowdhury, Z. Yan, S. M. Humphrey and T. Hutter, *Coord. Chem. Rev.*, 2023, **485**, 215119.
4 X. Zhou, X. Zhou, C. Wang and H. Zhou, *Chemosphere*, 2023, **313**, 137489.
5 Y. Xiong, K. Du and Y. Huang, *npj Clim. Atmos. Sci.*, 2024, **7**, 54.
6 C. Li, P. G. Choi and Y. Masuda, *J. Hazard. Mater.*, 2023, **455**, 131592.
7 J. Q. Xiao and S. M. Levin, *Am. J. Ind. Med.*, 2000, **37**, 44–61.
8 ATSDR, *Toxicological Profile for Acetone*, 2022.
9 X. Li, L. Zhang, Z. Yang, P. Wang, Y. Yan and J. Ran, *Sep. Purif. Technol.*, 2020, **235**, 116213.
10 C. Megías-Sayago, I. Lara-Ibeas, Q. Wang, S. Le Calvé and B. Louis, *J. Environ. Chem. Eng.*, 2020, **8**, 103724.
11 K. Dedecker, E. Dumas, B. Lavédrine, N. Steunou and C. Serre, in *Metal-Organic Frameworks (MOFs) for Environmental Applications*, Elsevier, 2019, pp. 141–178.
12 E. Gulcay-Ozcan, P. Iacomi, Y. Ko, J.-S. Chang, G. Rioland, S. Devautour-Vinot and G. Maurin, *J. Mater. Chem. A*, 2021, **9**, 12711–12720.
13 E. Gulcay-Ozcan, P. Iacomi, G. Rioland, G. Maurin and S. Devautour-Vinot, *ACS Appl. Mater. Interfaces*, 2022, **14**, 53777–53787.
14 M. I. Severino, A. Al Mohtar, C. Vieira Soares, C. Freitas, N. Sadovnik, S. Nandi, G. Mouchaham, V. Pimenta, F. Nouar, M. Daturi, G. Maurin, M. L. Pinto and C. Serre, *Angew. Chem., Int. Ed.*, 2023, **62**, e202211583.
15 P. P. Conti, K. Batra, P. Iacomi, C. V. Soares, S. Dasgupta, N. Steunou, A. Lattuati-Derieux, N. Timbart, M. Nicolas, R. Anton, S. Moularat, G. Maurin and S. Devautour-Vinot, *Chem. Commun.*, 2023, **59**, 7064–7067.
16 A. Becker, N. Israfilov, E. Ehrstein, I. Lara-Ibeas, J.-M. Planeix, B. Louis and S. Le Calvé, *Microporous Mesoporous Mater.*, 2022, **343**, 112136.
17 B. Kim, Y. R. Lee, H. Y. Kim and W. S. Ahn, *Polyhedron*, 2018, **154**, 343–349.
18 K. Yang, F. Xue, Q. Sun, R. Yue and D. Lin, *J. Environ. Chem. Eng.*, 2013, **1**, 713–718.
19 K. Yang, Q. Sun, F. Xue and D. Lin, *J. Hazard. Mater.*, 2011, **195**, 124–131.
20 A. F. Cosseron, T. J. Daou, L. Tzanis, H. Nouali, I. Deroche, B. Coasne and V. Tchamber, *Microporous Mesoporous Mater.*, 2013, **173**, 147–154.
21 Y. Pei, J. Qin, J. Wang and Y. Hu, *Sci. Total Environ.*, 2021, **790**, 148132.
22 X. Ren, S. Liu, R. Qu, L. Xiao, P. Hu, H. Song, W. Wu, C. Zheng, X. Wu and X. Gao, *Microporous Mesoporous Mater.*, 2020, **295**, 109940.
23 S. L. Griffin and N. R. Champness, *Coord. Chem. Rev.*, 2020, **414**, 213295.
24 J. R. Li, J. Sculley and H. C. Zhou, *Chem. Rev.*, 2012, **112**, 869–932.
25 M. J. Kalmutzki, N. Hanikel and O. M. Yaghi, *Sci. Adv.*, 2018, **4**(10), eaat9180.
26 M. Taddei and C. Petit, *Mol. Syst. Des. Eng.*, 2021, **6**, 841–875.
27 H.-C. Zhou, J. R. Long and O. M. Yaghi, *Chem. Rev.*, 2012, **112**, 673–674.
28 J. L. C. Rowsell and O. M. Yaghi, *J. Am. Chem. Soc.*, 2006, **128**, 1304–1315.
29 A. U. Ortiz, A. P. Freitas, A. Boutin, A. H. Fuchs and F. X. Coudert, *Phys. Chem. Chem. Phys.*, 2014, **16**, 9940–9949.
30 V. Bon, N. Kavoosi, I. Senkovska, P. Müller, J. Schaber, D. Wallacher, D. M. Többens, U. Mueller and S. Kaskel, *Dalton Trans.*, 2016, **45**, 4407–4415.
31 H. Reinsch, M. A. van der Veen, B. Gil, B. Marszalek, T. Verbiest, D. de Vos and N. Stock, *Chem. Mater.*, 2013, **25**, 17–26.

32 N. Sadovnik, P. Lyu, F. Nouar, M. Muschi, M. Qin, G. Maurin, C. Serre and M. Daturi, *Nat. Commun.*, 2024, **15**, 9456.
33 M. I. Severino, A. Al Mohtar, C. V. Soares, O. Kolmykov, C. Freitas, I. Dovgaliuk, C. Martineau, V. Pimenta, F. Nouar, G. Maurin, M. L. Pinto and C. Serre, *J. Mater. Chem. A*, 2023, **11**, 4238–4247.
34 D. Zhang, Y. Fan, G. Li, W. Du, R. Li, Y. Liu, Z. Cheng and J. Xu, *Sens. Actuators, B*, 2020, **302**, 127187.
35 J. Wang, J. Wu, B. Zheng, J. Wang, Q. Shi and J. Dong, *Chem. Eng. Sci.*, 2022, **248**, 117251.
36 J. J. Wardzala, J. P. Ruffley, I. Goodenough, A. M. Schmidt, P. B. Shukla, X. Wei, A. Bagusetty, M. De Souza, P. Das, D. J. Thompson, C. J. Karwacki, C. E. Wilmer, E. Borguet, N. L. Rosi and J. K. Johnson, *J. Phys. Chem. C*, 2020, **124**, 28469–28478.
37 H. Ito, S. Hashimoto and T. Katsuno, *ACS Appl. Eng. Mater.*, 2024, **2**, 1268–1277.
38 N. C. Burtch, H. Jasuja and K. S. Walton, *Chem. Rev.*, 2014, **114**, 10575–10612.
39 S. Xian, Y. Yu, J. Xiao, Z. Zhang, Q. Xia, H. Wang and Z. Li, *RSC Adv.*, 2015, **5**, 1827–1834.
40 Y. Li and R. T. Yang, *Langmuir*, 2007, **23**, 12937–12944.
41 T. T. Tung, M. T. Tran, J. F. Feller, M. Castro, T. Van Ngo, K. Hassan, M. J. Nine and D. Losic, *Carbon*, 2020, **159**, 333–344.
42 X. Zhang, Y. Wang, J. Mi, J. Jin and H. Meng, *Chem. Eng. J.*, 2023, **451**, 139000.
43 J. Cousin-Saint-Remi, A.-L. Finoulst, C. Jabbour, G. V. Baron and J. F. M. Denayer, *Microporous Mesoporous Mater.*, 2020, **304**, 109322.
44 L. Xie, M. Xu, X. Liu, M. Zhao and J. Li, *Advanced Science*, 2020, **7**, 1901758.
45 M. Zhu, P. Hu, Z. Tong, Z. Zhao and Z. Zhao, *Chem. Eng. J.*, 2017, **313**, 1122–1131.
46 N. Reimer, H. Reinsch, A. K. Inge and N. Stock, *Inorg. Chem.*, 2015, **54**, 492–501.
47 S. Ravichandran, M. Najafi, R. Goeminne, J. F. M. Denayer, V. Van Speybroeck and L. Vanduyfhuys, *J. Chem. Theory Comput.*, 2024, **20**, 5225–5240.
48 T. F. Willems, C. H. Rycroft, M. Kazi, J. C. Meza and M. Haranczyk, *Microporous Mesoporous Mater.*, 2012, **149**, 134–141.
49 D. Ongari, P. G. Boyd, S. Barthel, M. Witman, M. Haranczyk and B. Smit, *Langmuir*, 2017, **33**, 14529–14538.
50 G. Kresse and J. Hafner, *Phys. Rev. B: Condens. Matter Mater. Phys.*, 1994, **49**, 14251–14269.
51 G. Kresse and J. Furthmüller, *Comput. Mater. Sci.*, 1996, **6**, 15–50.
52 G. Kresse and J. Furthmüller, *Phys. Rev. B: Condens. Matter Mater. Phys.*, 1996, **54**, 11169–11186.
53 A. S. Rosen, S. M. Iyer, D. Ray, Z. Yao, A. Aspuru-Guzik, L. Gagliardi, J. M. Notestein and R. Q. Snurr, *Matter*, 2021, **4**, 1578–1597.
54 J. P. Perdew, K. Burke and M. Ernzerhof, *Phys. Rev. Lett.*, 1997, **78**, 1396.
55 S. Grimme, J. Antony, S. Ehrlich and H. Krieg, *J. Chem. Phys.*, 2010, **132**, 154104.
56 S. Grimme, S. Ehrlich and L. Goerigk, *J. Comput. Chem.*, 2011, **32**, 1456–1465.
57 G. Kresse and J. Hafner, *J. Phys.: Condens. Matter*, 1994, **6**, 8245.
58 T. A. Manz and N. G. Limas, *RSC Adv.*, 2016, **6**, 47771–47801.
59 N. G. Limas and T. A. Manz, *RSC Adv.*, 2016, **6**, 45727–45747.
60 T. A. Manz, *RSC Adv.*, 2017, **7**, 45552–45581.
61 N. G. Limas and T. A. Manz, *RSC Adv.*, 2018, **8**, 2678–2707.
62 T. J. H. Vlugt, E. García-Pérez, D. Dubbeldam, S. Ban and S. Calero, *J. Chem. Theory Comput.*, 2008, **4**, 1107–1118.
63 Q. Yang and C. Zhong, *J. Phys. Chem. B*, 2006, **110**, 17776–17783.
64 A. K. Rappé, C. J. Casewit, K. S. Colwell, W. A. Goddard and W. M. Skiff, *J. Am. Chem. Soc.*, 1992, **114**, 10024–10035.
65 S. L. Mayo, B. D. Olafson and W. A. Goddard, *J. Phys. Chem.*, 1990, **94**, 8897–8909.
66 A. Cadiau, J. S. Lee, D. Damasceno Borges, P. Fabry, T. Devic, M. T. Wharmby, C. Martineau, D. Foucher, F. Taulelle, C. H. Jun, Y. K. Hwang, N. Stock, M. F. De Lange, F. Kapteijn, J. Gascon, G. Maurin, J. S. Chang and C. Serre, *Adv. Mater.*, 2015, **27**, 4775–4780.
67 K. H. Cho, D. D. Borges, J. S. Lee, J. Park, S. J. Cho, D. Jo, U. H. Lee, G. Maurin and J. S. Chang, *ACS Sustain. Chem. Eng.*, 2022, **10**, 7010–7019.
68 D. Lenzen, J. Zhao, S.-J. Ernst, M. Wahiduzzaman, A. Ken Inge, D. Fröhlich, H. Xu, H.-J. Bart, C. Janiak, S. Henninger, G. Maurin, X. Zou and N. Stock, *Nat. Commun.*, 2019, **10**, 3025.
69 J. L. F. Abascal and C. Vega, *J. Chem. Phys.*, 2005, **123**, 234505.
70 J. M. Stubbs, J. J. Potoff and J. I. Siepmann, *J. Phys. Chem. B*, 2004, **108**, 17596–17605.
71 M. S. Shah, M. Tsapatsis and J. I. Siepmann, *Angew. Chem.*, 2016, **128**, 6042–6046.
72 S. Vandenbrande, M. Waroquier, V. Van Speybroeck and T. Verstraelen, *J. Chem. Theory Comput.*, 2018, **14**, 6359–6369.
73 V. Finsy, H. Verelst, L. Alaerts, D. De Vos, P. A. Jacobs, G. V. Baron and J. F. M. Denayer, *J. Am. Chem. Soc.*, 2008, **130**, 7110–7118.
74 W. A. Felsing and S. A. Durban, *J. Am. Chem. Soc.*, 1926, **48**, 2885–2893.
75 P. Z. Moghadam, D. Fairen-Jimenez and R. Q. Snurr, *J. Mater. Chem. A*, 2015, **4**, 529–536.
76 M. Thommes, K. Kaneko, A. V. Neimark, J. P. Olivier, F. Rodriguez-Reinoso, J. Rouquerol and K. S. W. Sing, *Pure Appl. Chem.*, 2015, **87**, 1051–1069.
77 J. Rouquerol, P. Llewellyn and F. Rouquerol, *Stud. Surf. Sci. Catal.*, 2007, **160**, 49–56.
78 C. C. Collados, C. Huber, J. Söllner, J.-P. Grass, A. Inayat, R. Durdyyev, A.-S. Smith, D. Wisser, M. Hartmann and M. Thommes, *Langmuir*, 2024, **40**, 12853–12867.
79 M. Thommes, J. Morell, K. A. Cychosz and M. Fröba, *Langmuir*, 2013, **29**, 14893–14902.
80 M. Thommes, S. Mitchell and J. Pérez-Ramírez, *J. Phys. Chem. C*, 2012, **116**, 18816–18823.